Available online at www.sciencedirect.com
SCIENCE DIRECT®
Analytical Biochemistry 346 (2005) 189–200
ANALYTICAL BIOCHEMISTRY
www.elsevier.com/locate/yabio

Quantitative atomic force microscopy image analysis of unusual filaments formed by the *Acanthamoeba castellanii* myosin II rod domain

Daniel J. Rigotti [a], Bashkim Kokona [a], Theresa Horne [b], Eric K. Acton [c], Carl D. Lederman [b], Karl A. Johnson [a], Robert S. Manning [c], Suzanne Amador Kane [b], Walter F. Smith [b], Robert Fairman [a,*]

[a] *Department of Biology, Haverford College, 370 Lancaster Ave, Haverford, PA 19041, USA*
[b] *Department of Physics, Haverford College, 370 Lancaster Ave, Haverford, PA 19041, USA*
[c] *Department of Mathematics, Haverford College, 370 Lancaster Ave, Haverford, PA 19041, USA*

Received 2 February 2005
Available online 19 September 2005

Abstract

We describe a quantitative analysis of *Acanthamoeba castellanii* myosin II rod domain images collected from atomic force microscope experiments. These images reveal that the rod domain forms a novel filament structure, most likely requiring unusual head-to-tail interactions. Similar filaments are seen also in negatively stained electron microscopy images. Truncated myosins from *Acanthamoeba* and other model organisms have been visualized before, revealing laterally associated bipolar minifilaments. In contrast, the filament structures that we observe are dominated by axial rather than lateral polymerization. The unusually small features in this structure (1–5 nm) required the development of quantitative and statistical techniques for filament image analysis. These techniques enhance the extraction of features that hitherto have been difficult to ascertain from more qualitative imaging approaches. The heights of the filaments are observed to have a bimodal distribution consistent with the diameters of a single rod domain and a pair of close-packed rod domains. Further quantitative analysis indicates that in-plane association is limited to at most a pair of rod domains. Taken together, this implies that the filaments contain no more than four rod domains laterally associated with one another, somewhat less than that seen in bipolar minifilaments. Analysis of images of the filaments decorated with an anti-FLAG antibody reveals head-to-tail association with mean distances between the antibodies of 75 ± 15 nm. We consider a set of molecular models to help interpret possible structures of the filaments.

Keywords: Myosin; Coiled coil; Rod domain; Atomic force microscopy

Many studies of myosin have revealed the formation of a higher order quaternary structure whose features are important for biological function. The ability to form such filaments is strongly dependent on electrostatic interactions, hence salt and pH must play critical roles in facilitating assembly. Though the higher order structure of different type II myosins is quite variable, a property conserved in all such molecules is their ability to self-associate into structures known as bipolar minifilaments [1]. Minifilaments are small complexes of usually 8–16 myosin monomers and have been observed in skeletal muscle [2,3], smooth muscle [4], and *Acanthamoeba castellanii* [1]. Minifilaments can self-associate to form yet higher order structures: in addition to the large-scale biological structures formed in muscle, paracrystals, which are much larger yet and involve extensive axial and lateral association, have been observed also [5].

The pathway and sequence determinants for bipolar minifilament formation have been well characterized in

* Corresponding author. Fax: +1 610 896 4963.
E-mail address: rfairman@haverford.edu (R. Fairman).

0003-2697/$ - see front matter © 2005 Elsevier Inc. All rights reserved.
doi:10.1016/j.ab.2005.08.026

the type II myosin from *A. castellanii* and are dictated by conserved electrostatic interactions between individual rod domains. Assembly is thought to involve a three-step process, proceeding initially through an antiparallel dimer intermediate, which can further self-associate to form tetramers and octamers. Under certain conditions, the octamers can further oligomerize to form "thick filaments" [6]. Specific sites of interaction in the *Acanthamoeba* myosin monomer that are responsible for each step of the self-assembly process to form the minifilaments have been identified. Sequences near the C-terminal end of the rod domain are known to be especially critical because chymotrypsin digestion, which targets the C terminus of the rod domain, prevents the assembly of bipolar minifilaments [7]. This has been confirmed more recently by antibody occlusion experiments using antibodies raised against peptides containing sequences from this same region of the rod domain [8,9]. Recombinant approaches have identified specific sequences responsible for the formation of each intermediate in the three-step self-assembly mechanism. A 20- to 30-amino-acid stretch in the nonhelical portion of the C-terminal end of the rod domain drives the initial antiparallel assembly of the dimer intermediate [10]. Formation of an antiparallel tetramer requires the last 40 residues within the coiled coil of the rod domain. Finally, 40–70 amino acids, also in the coiled coil, are known to be responsible for octamer assembly. In general, mutations in the regions responsible for specifying the pathway of assembly lead either to truncated assembly products or to alternative assembly products. Alternative assembly products, leading to protein–protein interactions that may be nonphysiological, are not surprising since electrostatic interactions can often lead to nonspecific aggregation in proteins. While the rod domain is sufficient for higher-order self-assembly [10], the globular headgroup of conventional myosin serves to control assembly for essential myosin II function in vivo. Without it, regulation of polymerization and function becomes problematic.

The myosin II monomer from *A. castellanii* is a conventional myosin composed of one pair of heavy chains and two pairs of light chains. The rod domain, which is ~90 nm long, is mostly helical, forming a long coiled coil, but contains a helix-breaking proline at about two thirds of its length from the amino terminus in the hinge region [11]. Aside from this section, the rod domain sequence largely obeys the rule of the heptad repeat $(abcdefg)_n$ for coiled coils, where positions *a* and *d* typically contain hydrophobic residues. A mutant from the Korn lab [12] that consists of the myosin II rod domain, without the globular head and hinge region and containing a deletion of a set of residues encompassing the proline ($\Delta_{384–408}$), was shown to form a continuous coiled coil based on sequence analysis and behaved largely as a single domain based on simple biophysical tests. In addition, it was shown that the deletion construct is mostly helical (~100%), exhibits two-state reversible folding, and exists as a monomeric coiled coil in fairly high salt (0.6 M KCl).

Here, we describe the use of this *A. castellanii* myosin II rod domain deletion mutant to develop quantitative methods for imaging long coiled coil systems by use of atomic force microscopy (AFM).[1] While a few papers describe the use of AFM to image myosin substructures [13–15], none have focused specifically on a study of self-assembly of the rod domains alone. The authors of these papers point out that the resolution of the images of individual myosin monomers are comparable to that seen previously by EM studies [16]. However, AFM offers the ability to image molecules without the need for metal shadowing or negative staining. We were particularly interested in identifying a model system in which we could easily study the monomeric form of truncated myosins containing only the rod domain for protein design purposes. But in the process of developing AFM as a tool for imaging of rod domain monomers, we also found conditions that led to the formation of filaments of unusual structure; the presence of such structures is also seen in EM images using negative staining, suggesting that the filaments are not simply an artifact of the AFM imaging procedure itself. The development of quantitative methods to analyze AFM images of these filaments is described, and the consequent implications for higher order assembly are discussed.

Materials and methods

Myosin purification

The myosin II rod domain of *A. castellanii* was obtained from the Korn lab and purified and stored as described previously [12]. Isopropyl-β-D-thiogalactoside-induced bacterial cultures containing the pFLAG-2 vector with myosin II rod domain $\Delta_{384–408}$ were broken open by sonication. Streptomycin (10%) was added to the supernatant to eliminate any residual nucleic acid activity. Ammonium sulfate (pH 7.5) saturation (65%) and dialysis into a Mg^{2+} buffer caused paracrystals to form and provided an effective purification tool. The protein was redissolved in a high-salt buffer (600 mM KCl, 10 mM Tris–HCl, pH 7.5) and the protein was run over an Octyl Sepharose (Amersham Pharmacia) column if needed. Protease inhibitors were added to prevent any degradation and were dialyzed out when the protein was to be used. If the protein was redissolved in buffer without salt after the Mg^{2+} precipitation, it was prone to aggregation; a visible precipitate formed after several hours which, when imaged by EM, revealed the presence of bipolar minifilaments.

Circular dichroism spectropolarimetry

CD data were collected on an Aviv 62A circular dichroism spectropolarimeter. Samples were prepared in 10 mM

[1] *Abbreviations used:* AFM, atomic force microscopy; EM, electron microscopy; CD, circular dichroism; SE, sedimentation equilibrium.

Tris–HCl, pH 7.5, and either 300 or 600 mM KCl, and measurements were taken using a bandwidth of 1.5 nm. Spectra were collected from 198 to 250 nm with a step size of 0.5 nm and an averaging time of 2 s. Thermal denaturations were collected from 2 to 98 °C at 222 nm, with a step size of 2 °C, an averaging time of 30 s, and a time delay of 2 min.

Analytical ultracentrifugation

Protein samples were prepared in 10 mM Tris–HCl, pH 7.5, and 300, 600, and 900 mM KCl. All sedimentation equilibrium (SE) experiments were carried out at 4 °C using a Beckman Optima XL-A analytical ultracentrifuge equipped with an An60 Ti rotor and using six-channel, 12-mm-path-length, charcoal-filled Epon centerpieces and quartz windows. The loading concentration for the myosin II rod domain was 2 μM (0.14 mg/ml). Data were collected at two rotor speeds (8000 and 11,000 rpm) and represent the average of 20 scans using a scan step size of 0.001 cm. Partial specific volumes and solution density were calculated using the Sednterp software [17]. Data were truncated using the WinReedit (v. 0.999) program (1998) and analyzed using the WinNonLin (v. 1.035) program (1997) [18].

Atomic force microscopy

Samples for AFM imaging were prepared by depositing 20 μl of myosin solution (2–18 μM in 10 mM Tris–HCl, pH 7.5, 100–900 mM KCl) onto 0.25×0.25 in. freshly cleaved mica. The samples were then incubated in a constant humidity chamber for ~10 min, rinsed with sterile water for ~30 s, and blown dry. Samples were imaged in tapping mode using a Digital Instruments Bioscope AFM, with standard etched silicon probes (Nanodevices, Santa Barbara, CA).

Electron microscopy

Myosin II rod domain samples (2 μM) in 10 mM Tris–HCl, pH 7.4, 300 mM KCl were adsorbed to carbon-coated, formvar-covered 400-mesh copper EM grids (Electron Microscopy Sciences, Ft. Washington, PA) that had been pretreated by glow discharge and/or polylysine coating to improve sample adherence and stain retention. The samples were then rinsed briefly with distilled water and negatively stained with NanoVan (Nanoprobes, Yaphank, NY), a fine-grained, vanadium-based contrasting agent. Samples were imaged on an Hitachi H-600 electron microscope (Hitachi, Tokyo, Japan) operating at 75 keV equipped with a Gatan 789 camera (Gatan, Warrendale, PA).

Preparation of myosin II rod domain bound to M5 anti-FLAG monoclonal antibody

Since the M5 anti-FLAG monoclonal antibody (Sigma) had such high affinity for the N-terminal FLAG sequence, a 1:1 stoichiometry (myosin molecule:antibody molecule) was used. To 80 μl of 2 μM myosin (0.15 mg/ml), 6.9 μl of M5 antibody was added (3.5 mg/ml). The solution was incubated at room temperature for 30 min as recommended by the vendor. This procedure was preferable to probing mica-bound myosin with antibody since the antibody binds the mica surface readily and could potentially interfere with the image analysis of the myosin filaments.

Image processing

AFM images of the protein filaments were analyzed using both SigmaScan Pro 5.0 (SPSS, Chicago, Il) and ScionImage (Scion, Frederick, MD). Subsequent data analysis involving fitting and statistical analyses were performed using Origin 7.0 (OriginLab, Northhampton, MA) and Mathematica 5.0 (Wolfram Research, Champaign, IL). Images to be analyzed were first smoothed using a 3×3 pixel-averaging filter to remove single pixel noise (we found that this did not significantly alter the heights obtained). The images were then calibrated using the known AFM in-plane and z dimensions (where the z direction is defined as perpendicular to the imaging plane). All AFM images were 512×512 pixels, so pixel sizes ranged from 0.98 to 1.95 nm (for 500-nm to 1-μm square images). The 8-bit grayscale intensity at each pixel corresponded to a height range of 10 nm for myosin-only images and 25 nm for images containing antibodies.

Results

The *Acanthamoeba* myosin II rod domain $\Delta_{384–408}$ mutant (residues 384–408, containing a proline-rich hinge, have been deleted) was expressed as a fusion product with an amino-terminal FLAG sequence and purified as described previously [12] with minor modifications. We refer to this mutant throughout simply as the myosin II rod domain. The stability and reversibility, as measured by temperature denaturation using circular dichroism as a probe (data not shown), are consistent with previously published reports [12]. Our CD analysis shows that the myosin II rod domain is mostly helical under a variety of different conditions, consistent with a structure dominated by a coiled coil motif. Intending to use the myosin II rod domain for protein design experiments, we explored salt conditions that would favor monomers.

Analytical ultracentrifugation

Sedimentation equilibrium analytical ultracentrifugation (Tables 1 and 2) was performed to determine the size and polydispersity of the myosin II rod domain in several different salt conditions. The myosin rod domain forms a stable coiled coil [12], so the smallest species observed is consistent with the molecular weight expected of the coiled coil, which is twice the polypeptide chain molecular weight. The apparent molecular weight, from an analysis of data collected at two different speeds (8000 and 11,000 rpm), revealed an increase

Table 1
Molecular mass analysis of myosin II rod domain as measured by equilibrium sedimentation

[KCl] (mM)	Speed (rpm)	
	8000	11,000
300	277,840[a]	217,300
600	246,560	188,540
900	241,890	180,160

Data were collected at 4 °C. The monomer rod domain molecular mass is 151,802 Da.
[a] All results are in Daltons.

Table 2
Model analysis of myosin II rod domain as measured by equilibrium sedimentation

Model	Model analysis[a]		
	300 mM	600 mM	900 mM
Single species	9.09	9.30	6.71
Monomer[b]	13.52	12.23	8.12
Dimer	11.42	16.30	11.50
Trimer	20.75	28.76	19.80
$1^{b} \leftrightarrow 2$	8.33	8.50	6.38
$1 \leftrightarrow 3$	6.94	7.63	6.02
$1 \leftrightarrow 4$	5.82	7.15	5.79
$1 \leftrightarrow 10$	3.91	5.31	6.63

[a] Results are reported as the square root of variance ($\times 10^{-3}$) between the data and the model being considered.
[b] Monomer corresponds to one molecule of *Acanthamoeba* myosin II rod domain.

in myosin II rod domain filament size with decreasing KCl concentration (Table 1). This result is consistent with previous findings on the dependence of assembly on salt concentration. We also note a rotor speed dependence on the apparent molecular weight calculated assuming a single species. This is a useful diagnostic for polydispersity, as larger species tend to sediment out of the window of observation, resulting in an apparent decrease in molecular weight with rotor speed. In fact, the residuals from fits of the data collected at different salt concentrations using a single species model were nonrandom, further supporting polydispersity in filament size. In considering more complex models, we found some improvement in the quality of the fits, suggesting at least two states, with one state being the monomer form of the rod domain. However, we found no unique set of oligomeric states for the self-associating species presumably because the filaments are too polydisperse (Table 2). Nevertheless, we can draw some conclusions from the model analysis about limiting sizes. In the case of high salt (900 mM), we find that the quality of the fit to the data is best for a $1 \leftrightarrow 4$ model. At lower salt concentrations, the second state was modeled best by higher order oligomeric states with an oligomeric state of 8 giving the best fit, consistent with that expected for bipolar minifilaments. These results were used to define solvent conditions to favor the monomer form in our subsequent AFM experiments.

AFM images

To prepare samples for AFM imaging, we used 2 μM solutions of myosin II rod domain (the same concentration as that used in the analytical ultracentrifugation experiments) at various salt concentrations to explore the dependence of filament formation on salt (Fig. 1). As expected, we observed an increase in the fraction of rod domains participating in filament formation with decreasing salt concentration. This can be seen visually by comparing the relative amounts of myosin forming long filaments with that forming much shorter structures in 300 vs 600 mM KCl (Fig. 1). Using even lower salt concentrations results in such a high concentration of long filaments that individual filaments can no longer be readily discerned in AFM images.

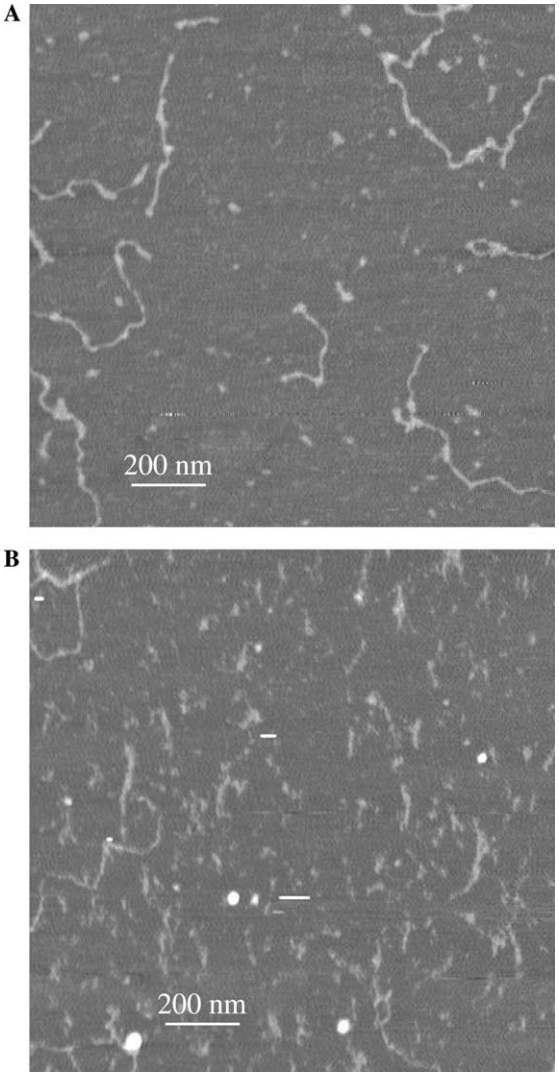

Fig. 1. Myosin II rod domain imaged by AFM under different salt concentrations. Protein concentration is 2 μM. Buffer conditions are 10 mM Tris–HCl, pH 7.4, and 300 mM KCl (A) and 600 mM KCl (B). All images are taken by tapping mode AFM showing fields of myosin adsorbed onto a mica substrate. Both images are 1 μm square.

Surprisingly, the filaments observed in the AFM images were different from those observed for the intact myosin II, which form bipolar minifilaments, or for other variants of rod domain truncations, which can form different intermediates in bipolar minifilament assembly [6]. Most of the structures that we found were thin filaments of varying length that are assembled axially with little evidence for extensive lateral association, as might be seen in paracrystals. Given the unusual nature of the filaments, we wanted to confirm that the images were indeed that of myosin II. We tested the samples for sensitivity to both protease and DNase digestion. Treatment of samples before mica deposition with proteinase K completely eliminated the long filaments, whereas treatment with DNase 1 had no effect (data not shown). Finally, we were able to show specific binding to the filaments on the surface of the mica using an anti-FLAG antibody (Fig. 5A). We cleaved the FLAG sequence from the myosin fusion construct using a built-in enterokinase site, redialyzed the samples to remove the FLAG-Tag, and found that the unusual filament formation was still present, indicating that filament formation was not significantly influenced by the presence of this fusion partner.

Having shown that the filaments were indeed made up of myosin rod domains, we wondered whether the filaments might be an artifact of deposition onto a mica surface. To test this, we deposited the myosin rod domains under the same sample preparation conditions (300 mM KCl) onto carbon-coated copper grids and imaged them by EM after negative staining (Fig. 2). Despite the small diameter of the rod domains being close to the limit of resolution of the negative stain contrasting technique, it was possible to discern individual rod domains using NanoVan staining, a vanadium-based contrasting agent that yields a finer grain than uranyl acetate. The ability to identify individual rod domains in the EM images (Fig. 2A) is comparable, if not better, than that seen previously for myosin fragments (with intact head domains) [16]. In addition to the individual rod domains, we also observed longer filaments (Figs. 2B and C) very similar in dimension to the filaments that we observed in our AFM images (Fig. 1).

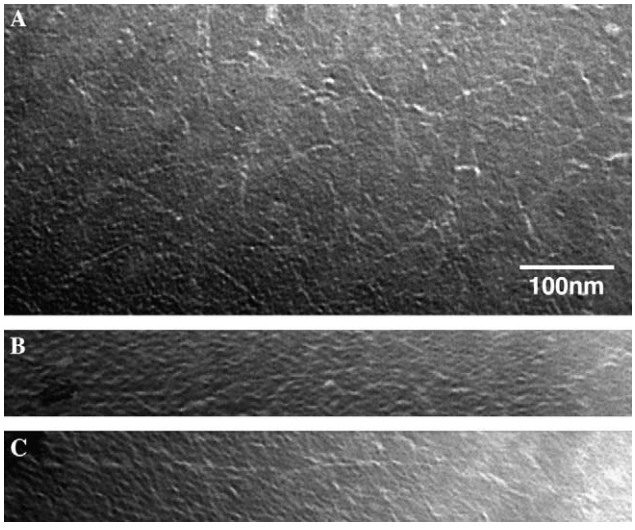

Fig. 2. Negatively stained electron microscopic images of myosin II rod domain preparations. Protein samples (2 μM) in 10 mM Tris–HCl, pH 7.4, 300 mM KCl were adsorbed to carbon-coated EM grids and negative stained. Numerous, thin, filamentous structures of 70- to 80-nm unit lengths are apparent (A), as are longer linear arrays (B, C). Scale bar is 100 nm for all panels.

The AFM images selected for further analysis were representative of all the images collected but we particularly focused on fields that were not as crowded so that the features of individual filaments could be better highlighted. We performed this analysis for the 300 mM KCl conditions, where the axial association is more prominent.

The surface roughness of the mica surface is a critical lower bound for the precision of all height measurements. The height distributions of bare-mica regions were consistently well fit by Gaussians. The center of the Gaussian gives the base-line height of the mica for each sample; the exact value in nm is arbitrary and is set by the definition of the z-alignment of the AFM. The standard deviation of the Gaussian, which describes the roughness of the mica, was consistently ~0.15 nm (a value comparable to the z-resolution of our instrument).

Analysis of filament lengths

We focus initially on an analysis of length distributions, which were determined using SigmaScan as follows. First, any pixel in the image with a height sufficiently above average (0.30 nm = 2 SD of mica surface) was tagged as a possible filament pixel. To smooth the images on single-pixel-length scales, two rounds of an erosion filter and then two rounds of a dilation filter were applied. Second, the pixels in the processed image were grouped into objects so that adjacent pixels belonged to the same object. All distinct objects were included in the analysis if their areas exceeded the size range expected for individual rod domain monomers. Furthermore, a small number of very high regions were ignored as these are almost certainly salt crystals; they are significantly wider than the protein filaments and become less prevalent with increased rinsing of the sample. We found no particular preference for a given length in the protein filaments; the histogram of number fraction vs filament lengths exhibited a smooth decay with length. This distribution agrees in general with those predicted by theories of step-polymerization [19] or fragmentation [20].

Analysis of filament heights

To determine the distribution of heights within the filaments, AFM images were analyzed by tracing all filaments in an image by hand using SigmaScan (Fig. 3A). The resulting histogram of heights along the filaments was well fit by a double-Gaussian distribution in Origin, as shown in Fig. 3B. Thus, two distinct height distributions emerged

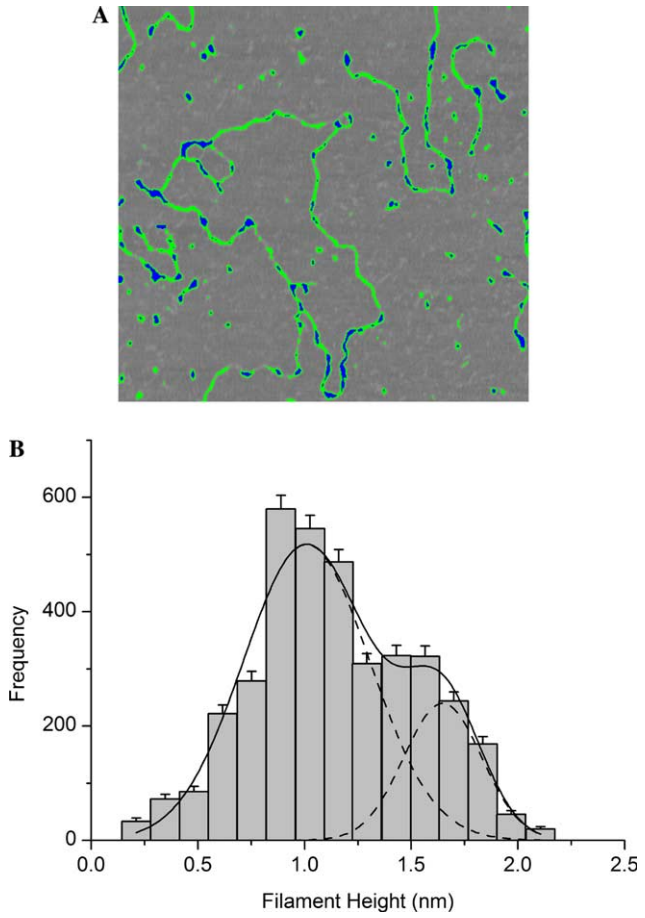

Fig. 3. (A) Typical AFM image (1 μm square) of filaments formed from myosin II rod domain, with the mica substrate indicated by grayscale, and filaments consistent with one and two rod domain high filaments indicated by green and blue, respectively. (B) Filament height distribution. A trace is made along the length of a filament and a bimodal distribution of filament heights corresponding to two peaks with average heights of 0.96 and 1.57 nm (consistent with single-height and double-height regions as explained in the text) was seen.

from this analysis, which we call single-height and the double-height regions. The midpoint between these two Gaussians was used as a threshold between the single-height and double-height regions. The lower threshold for the single-height region was taken to be two standard deviations above the mica substrate level. For example, in Fig. 3A, single-height regions are shown in green and double-height regions in blue. The first of the two Gaussians is centered at a height of 0.96 ± 0.06 nm (error bars are determined by sampling over multiple different images). This value of 0.96 nm is thus the primary filament height observed in the samples and is consistent with the 1.5-nm diameter of a coiled coil. It is typical for the AFM-measured height of macromolecules to be somewhat less than the height expected from solution conditions, due to interactions with the substrate and compression of the molecule by the AFM tip [21]. The standard deviation of this first Gaussian peak is ~0.3 nm and reflects, in part, local variations in substrate–filament interaction (note that half of this variation can be attributed to the roughness of the underlying substrate). The second Gaussian peak is centered at a height of 1.57 ± 0.04 nm, which is approximately equal to the height of 1.79 nm expected for a two-layer bundle of 0.96-nm rod domains that are close packed. The standard deviation of this second peak is ~0.2 nm. Many of these double-height regions appear to occur at crossing points between two single-height strands or at regions where a single strand appears to loop back on top of itself. However, there are also double-height regions that appear to emerge in the middle of a single-height region. Overall, approximately 80% of the filaments are single-height regions, with the remainder being double-height regions.

Analysis of filament widths

The in-plane widths of single-height regions seen here in tapping mode AFM are 10–15 nm, which is consistent with previous in-plane measurements of monomeric myosin of 10–16 nm [15]. Unfortunately, the anticipated broadening due to convolution of the small (<2 nm) features of the myosin II rod domain monomers with the wider-radius AFM tip [22,23] makes a more accurate determination of the in-plane filament width problematic. We found that the double-height regions were consistently wider than the single-height regions as shown in the height–width profiles in Fig. 4A. Such broadening may be caused by in-plane lateral association. However, it is just as likely that tip convolution would broaden the AFM trace of a double-height region more than a single-height region even if they were actually the same width. Calibration of the tip using existing standards, such as Nioprobe samples (Digital Instruments, Santa Barbara, CA) or gold nanospheres (Ted Pella, Redding, CA) did not yield useful calibration information, both because of the small length scales of interest here and, in the case of the gold spheres, because they appeared to coat the AFM tip and thereby corrupt future images.

Nevertheless, we were able to find a range of plausible filament widths using mathematical modeling. Cross-sectional height profiles were chosen by hand uniformly through one 500-nm image: 17 profiles over single-height regions and 16 profiles over double-height regions. These profiles were fit to single Gaussians in Origin to determine the average mica height and center of the myosin filament peak in the profile. The difference between the maximum height in the profile and the average mica height was taken to be equal to the diameter of the filament for single-height regions and equal to $1+\frac{\sqrt{3}}{2}$ times the diameter for double-height regions, according to the geometry of close-packed cylinders (where cylinders are assumed to be reasonable approximations of individual rod domains). The radius of the AFM tip was determined by a least-squares fit in Mathematica to a functional form that extends the single-cylinder model [24] to multiple cylinders. This model involves the convolution of a hemispherical tip with the chosen model for myosin filaments, either a single layer or a double close-packed layer of one to four side-by-side cylinders.

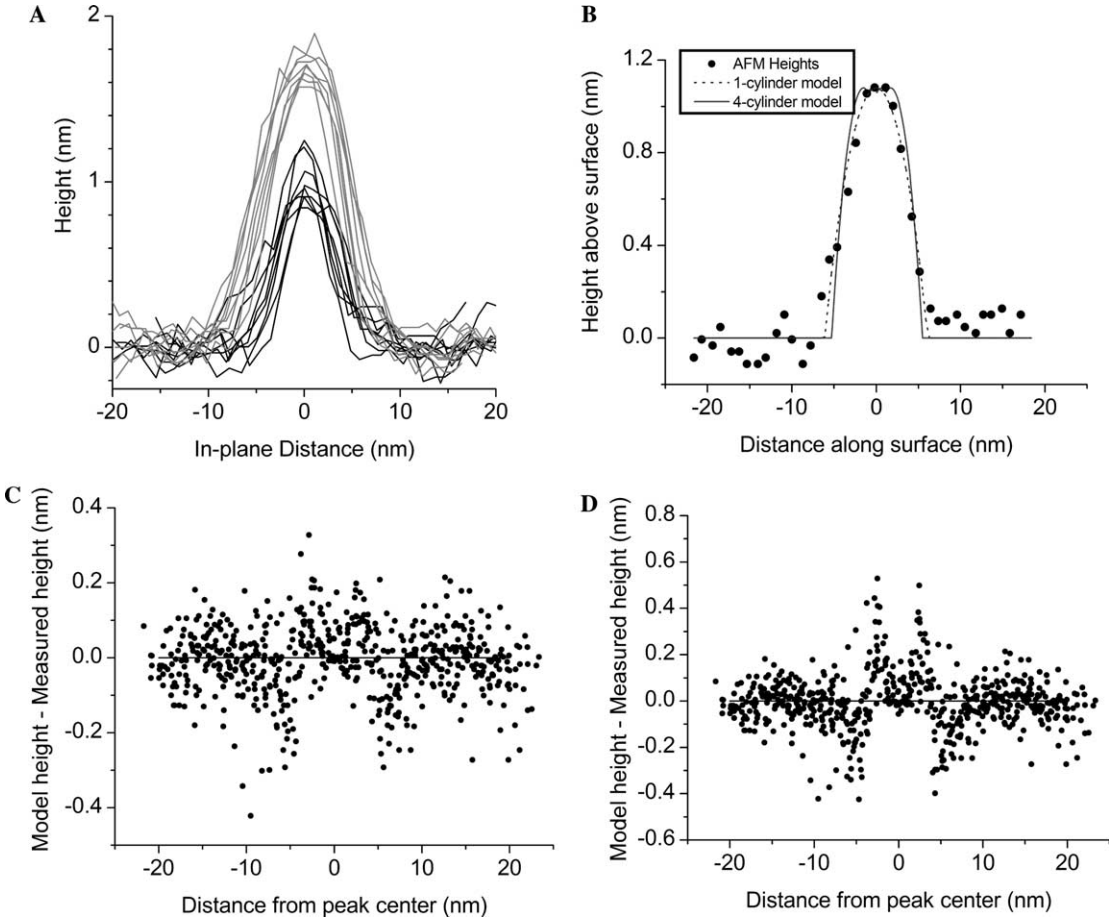

Fig. 4. Analysis of in-plane widths (A) Eight typical cross-sectional height vs in-plane distance profiles for single-height (black lines) and double-height (gray lines) regions. (B) Best-fit height profiles using a single-cylinder (black line) or a four-cylinder (gray line) model to a cross section of a single-height region (dots). (C, D) Residuals for the aggregate best-fit analysis of 17 single-height profiles are more uniform for the single-cylinder model (C) than for the four-cylinder model (D).

The results from the cross-sectional analysis are shown in Table 3. Thus, for the single-height regions, we find a notable drop in the quality of fit when we go to a four cylinder model, dropping the p value below the usual range of acceptability. We also see a better fit for the one-cylinder model than for the two- or three-cylinder models, though in all three cases we see p values in the acceptable realm. As an illustration, we consider the difference between the one-cylinder and the four-cylinder fits. The χ^2 value was lower in the one-cylinder case in all but 1 of the 17 traces; a paired t test on the changes in χ^2 values indicates that the changes are significant ($p < 0.005$). In addition, the best-fit profiles from a 1 cylinder model were more reasonable than those seen using the four-cylinder model. The fits in Fig. 4B correspond to the dataset with the median % change in χ^2. It is apparent that the four-cylinder best-fit traces are more rectangular than the measured data, whereas the one-cylinder versions are consistently closer to the correct shape. This is confirmed by the residual errors for all 17 traces, shown in Figs. 4C and D, where the bias around the peak center is apparent in the four-cylinder case and less pronounced in the one-cylinder case. Nevertheless, there is a significant nonrandom component to the residuals in the one-cylinder case: this is probably due to the fact that the peaks in the AFM traces have ''shoulders.'' These shoulders may be due to extensive hydration or variations in the AFM tip shape; such possibilities were not included in the theoretical model. As a result, the best-fit trace expands slightly to capture a portion of the shoulders, and this means that it is slightly too wide in the main portion of the peak. Finally, the best-fit values for the AFM tip radius are more plausible in the one-cylinder case (median $R = 13.7$ nm) than in the four-cylinder case (median $R = 5.4$ nm). Indeed, in the four-cylinder case, in 4 of the 17 traces analyzed, the best-fit AFM tip radius was less than 2 nm, an unrealistically small value.

A similar analysis was carried out on the double-height regions, varying the number of cylinders in the top layer (the AFM tip never interacts with the bottom layer, so our model is insensitive to its structure). While the double-height regions have broader AFM traces (as pointed out above), this could be due either to tip broadening for double-height regions or to additional lateral association. Our mathematical model allows us to address this question. The cylinder diameter was determined from the maximum height of the AFM trace. The results of this

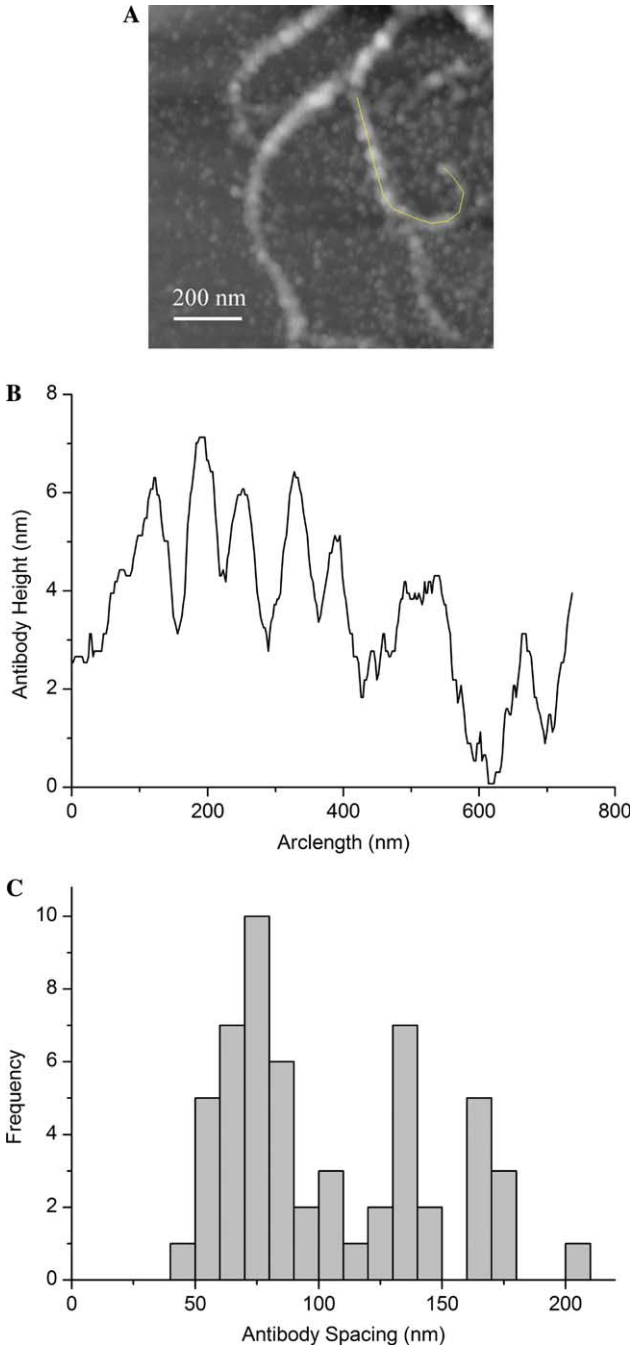

Fig. 5. (A) AFM image of myosin II rod domains decorated with the anti-FLAG antibody. The image is presented at the same scale as the images shown in Fig. 3. The sample is in 300 mM KCl, 10 mM Tris–HCl, pH 7. (B) Height vs in-plane distance plot along a typical filament in the antibody images. (C) Histogram showing the distribution of spacing between antibodies along the filament backbone, indicating a strong peak with an average spacing of 75 ± 15 nm.

analysis were analogous to the single-height results, as is shown in Table 3. The data were once again best fit by the one-cylinder model, although we note that the overall quality of fit is poorer in this case, which makes sense since the higher filament will sample more of the AFM tip and thus the simple hemispherical tip model is less likely to be accurate. In this case, the quality of fit seems to deteriorate fairly regularly, with the median p value dropping by two orders of magnitude with each additional cylinder. We thus are confident in rejecting the three- and four-cylinder models but, given the overall poorer quality of all the fits, we cannot reject the two-cylinder model, despite its low p value.

Table 3
Model analysis of the widths of myosin filaments imaged by tapping mode AFM

No. cylinders	Median reduced χ^2	Median p value	Median best-fit tip radius (nm)
Single-height regions			
1	1.0	0.43	13.7
2	1.4	0.09	10.2
3	1.4	0.07	7.5
4	1.7	0.006	5.4
Double-height regions			
1	1.6	0.01	15.1
2	1.8	0.0009	12.8
3	2.3	9×10^{-6}	10.6
4	2.7	4×10^{-8}	8.8

Antibody analysis of filaments

We took advantage of the FLAG-Tag fusion partner to map out the aminoterminal ends of the monomer units within the filaments and to determine whether the rod domain interactions reflect parallel or antiparallel orientations. Myosin filaments were incubated with an anti-FLAG antibody and deposited on a mica surface in a fashion similar to that of our previous experiments. The antibody does not appear to influence the overall filament structures since the filaments appear similar to images collected without antibody present. Many filaments within a single AFM image were highly decorated (Fig. 5A). To provide further evidence that the punctuated decoration is due to antibody binding, we compared the average height and in-plane dimensions of AFM images of antibodies on bare mica to these features. To determine average antibody sizes, height profiles from 10 antibodies bound to mica were collected and the heights extracted using Gaussian fits; the same procedure was applied to 12 antibodies bound to filaments. Antibodies bound directly to mica appeared as approximately globular objects 7.0 ± 0.8 nm high (data not shown). The expected height for an antibody binding to a surface depends largely on the number of domains engaged in surface binding. We calculate a range of 6.5–16 nm assuming several modes of binding, with a value of 8.5 nm assuming engagement of only the combining site with the surface and flexibility about the Fc-Fab hinge. We suspect that this specific case predominates since this height is most consistent with the average measured height of 7.0 nm, assuming typical compression forces exerted by the AFM tip. Antibodies bound to myosin filaments had similar, but slightly larger, heights of 7.5 ± 0.8 nm, consis-

tent with complex formation between the antibody and the underlying myosin rod domain.

The density of antibody on individual filaments was such that we were able to quantify accurately the distance between individual antibody molecules. For determination of the antibody spacing along the filament, height vs in-plane distance profiles were collected by tracing along the filament by hand (Figs. 5A and B). Next, the automated peak-finding feature in Origin was used to determine the distribution of distances between adjacent antibodies along the filaments. The peaks identified in this fashion largely agreed with visual inspections. All features identified as peaks were included in the statistical analysis, and the distances between adjacent peaks were computed. Fifty such distances were recorded from different filaments drawn from three separate AFM images. A histogram of the distribution of these distances was approximated well by a Gaussian function. To determine the average distance between antibodies along the filament, the average and standard deviation of all data with spacings less than or equal to 110 nm were computed. A similar analysis performed on height variations on the mica substrate revealed a flat distribution of in-plane spacings, ruling out a nonspecific origin for this modulation. The average distance between the most closely spaced antibody peaks was 75 ± 15 nm, with an additional peak at approximately twice that value (consistent with the automatic peak-picker occasionally missing a peak), as seen in a histogram of the distribution of average spacings (Fig. 5C). EM images of individual myosin rod domain monomers from our own work (Fig. 2) and from the Pollard group [1] reveal average lengths consistent with the findings from our antibody experiments.

Discussion

One of our goals was to develop AFM methods for image analysis of long coiled coils and we chose the *Acanthamoeba* type II myosin rod domain as a model system. In the process of identifying conditions favoring the monomer (or disassembled) form of the protein, we found that the rod domain formed unusual filamentous structures, as seen in both AFM and EM images. We focused our efforts to develop quantitative AFM tools for image analysis of such thin filaments. This quantitative treatment has allowed us to assess the relationship in the interactions between individual monomers that we observe to that seen in bipolar minifilament intermediates.

Specifically, we chose to analyze AFM images of the myosin rod domain in 300 mM KCl based on our solution studies using sedimentation equilibrium experiments. Higher salt concentrations proved problematic due to the increasing number of salt crystals deposited on the mica surface and obscuring the myosin filaments. In 300 mM KCl, SE experiments suggest that the rod domains are largely monomeric although there is evidence for some self-assembly consistent with the molecular weight expected for a tetrameric intermediate in bipolar minifilament assembly. However, since SE experiments do not give shape information, we cannot readily distinguish minifilaments and the longer filaments that we observed by AFM. While sedimentation velocity experiments can resolve issues of macromolecular shape in solution, absorbance artifacts from the purification protocol prevented such an analysis. Since the degree of self-assembly in both the SE and the AFM experiments are salt dependent, we infer that the structures in the AFM images are also stabilized by electrostatic interactions as seen with bipolar minifilaments. Disparity between the SE and the AFM results suggest one of two possibilities: either (1) surface effects drive the formation of long filaments from the available pool of monomers (under the salt conditions used, monomer was present in the SE experiments) due to extensive but weak association with the mica or (2) the long filaments are present in solution but at very low concentration and, under the deposition conditions, the long filaments preferentially bind, again due to the ability to form extensive weak interactions with the mica. In either case, since we see such filaments by EM also, it is unlikely that specific properties of the mica are the major driving force; rather general surface properties (i.e., local surface salt and protein concentration effects) may be prevalent. This issue remains unresolved and will require further study.

Given the unprecedented nature of the filaments, we were concerned that the fusion partner may play a role in favoring assembly in the axial direction. However, we ruled out this possibility because removal of the FLAG-Tag by enterokinase digestion did not affect the formation of filaments. In addition, one might expect that the solution binding of the antibody to the fusion protein would occlude participation of the FLAG sequence in polymerization, thus further supporting the conclusion that sequences intrinsic to the rod domain are responsible for the unusual filament structures that we observe.

We were interested in determining the extent of lateral association in the filament structures to determine whether they were related to any intermediates in bipolar minifilament assembly. We focused first on measuring the z axis heights of the filaments since, for AFM, these measurements are much more accurate than in-plane measurements. Such measurements revealed a distribution of single-height and double-height regions, consistent with the expected heights of a single rod domain (dominated by the coiled coil motif), and two rod domains in close juxtaposition, respectively. This distribution argues against the presence of bipolar minifilaments as units in the assembly of the longer filaments; such structures would be too large, requiring at least four rod domains in any given lateral dimension.

In-plane measurements are typically inaccurate due to convolution of the AFM probe with the molecule under study [23]. The 10- to 15-nm width that we observe for these filaments, while being consistent with previous work [15], does not allow us to formally rule out limited in-plane lateral association. Although this width suggests that our

filaments are not aggregated significantly in the lateral dimension, we sought to test this explicitly by quantitative analysis of the AFM images. Using simple mathematical models assuming cylinders for the shape of the rod domains, we found that the in-plane widths were best fit with models describing either one or two rod domains, again being inconsistent with bipolar minifilament assembly (requiring at least a four-cylinder in-plane distribution), and agrees with the conclusion reached from the *z* axis analysis. These widths agree with those seen in the EM images, although the widths of the filaments are at the lower limit of the resolving ability of the EM (<5 nm). Given problems with resolution, we did not attempt to quantify the widths of the filaments using the EM images.

Given the measured degree of lateral association in both the *z* axis and the in-plane dimensions, we considered two dimer intermediate models from the literature whose widths are consistent with our measurements. While other models can be envisioned (i.e., different degrees of stagger between pairs of rod domains), we focus only on models for which a precedent exists. Parallel [7,10,25] and antiparallel [6] dimer intermediates have been observed previously, thus it is possible that the filaments represent axial assembly of either of these intermediates, as schematized in Fig. 6, in which each cylinder represents a single rod domain (or single coiled coil). In general, for such filaments, the single height regions that we observe would require association between rod domains only in the plane of the mica (Fig. 6). In the case of antiparallel dimer intermediates, the overlap between rod domains is only about 15 nm [6]. Thus, the double-height regions must reflect lateral association between individual filaments (Fig. 6A). For filaments containing parallel dimer intermediates (Fig. 6B), where the overlap is much greater (about 75 nm) [10], the double-height regions may reflect a twisting of the filament so that the association between dimer intermediates is now stacked along the *z* axis. Alternatively, the rod domains within the dimer intermediates may still interact with one another within the plane of the mica, and a second filament made up of similar dimer intermediates now lies on top of this first structure, providing a bundle that may be similar to the tetramer intermediate observed previously [6]. We favor the second model, involving parallel dimers, since the domain that helps to stabilize the antiparallel dimers is not present in this construct. Furthermore, similar constructs lacking this domain have been shown to form largely parallel dimer intermediates [10]. There are two ways in which parallel dimers can lead to filament formation: dimer intermediates can associate either through head-to-tail interactions (Fig. 6B) or through alternating head-to-head and tail-to-tail interactions. Our antibody experiments address this question.

We show that an anti-FLAG-Tag antibody decorates the filaments with regular periodicity and with an average distance between antibodies of 75 nm. In the case of the antiparallel dimer, which is a well-accepted intermediate in bipolar minifilament assembly, the rod domains overlap by only a short region (about 15 nm) at the C-terminal domain (Fig. 6A). In such a model, requiring both tail-to-tail and head-to-head interactions to form the filaments that we observe, we would predict a periodicity of antibody binding of 2×75 or 150 nm; we do not see evidence for such a distribution. It is possible to obtain a periodicity of 75 nm in the spacing of antibodies in an antiparallel model if one assumes an overlap of 50% in the dimer intermediate; we cannot rule out this structure, but there is no precedent in the literature for such a structure. The role of parallel dimer intermediates in myosin assembly has been more controversial [25] although recent work on *Acanthamoeba* myosin rod domains has provided clear evidence for parallel dimers

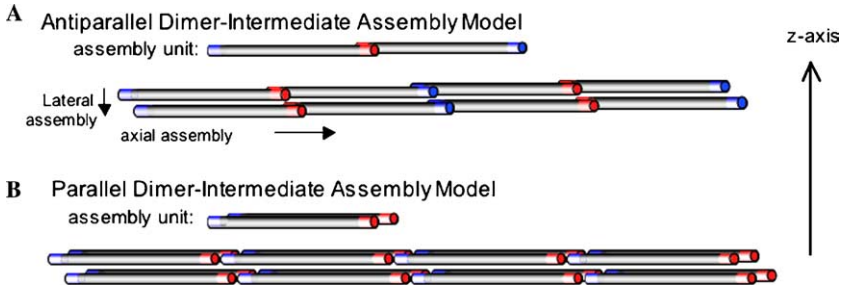

Fig. 6. Two models illustrating interactions between rod domain monomers and their higher order filament associations to form fibrils. Each rod domain (or coiled coil) monomer is represented as a cylinder and is color coded blue at the amino terminus and red at the carboxy terminus to indicate directionality. In-plane interactions in the AFM experiments are orthogonal to the plane of the figure, with the *z* axis being along the plane of the figure, as illustrated by the *z* axis arrow to the right of the models. (A) The antiparallel dimer intermediate assembly model assumes that the initial interactions are those involved in bipolar minifilament assembly, namely antiparallel association of the C termini. The assembly unit would then form additional antiparallel interactions at the N termini to give rise to filaments. In such a model, double-height regions in the AFM images would require association of two filaments along the *z* axis, as suggested in the scheme immediately below. It is possible that two filaments are associating in the *xy* plane also since we could not distinguish between one-cylinder and two-cylinder models in our mathematical analysis of in-plane widths. (B) The parallel dimer intermediate assembly model assumes a 75-nm overlap (leaving 15-nm staggered ends) as described earlier [10]. In this model, individual parallel dimers might form head-to-tail interactions. Double-height regions in the AFM images may be a reflection of either twisting of an individual filament or regions where two filaments might be associating along the *z* axis. In either the antiparallel or the parallel dimer assembly models, given the uncertainty in our *xy* plane measurements, the upper limit in lateral assembly is two rod domains for the single-height regions and four rod domains for the double-height regions.

which overlap over most of their rod domains, leaving 15 nm overhangs on either end [10]. There are two ways that such intermediates can assemble, involving either only head-to-tail interactions (Fig. 6B) or alternating tail-to-tail and head-to-head interactions. Head-to-tail interactions in these parallel dimer intermediates are particularly attractive in light of our antibody binding experiments since the 15 nm overhangs would result in antibody spacings consistent with our observations and would show regular periodicity. In addition, work from the Pollard group [10] has provided evidence for interactions involving proximal ends of the rod domain (the N-terminal end), thus providing further support for this model as driving the assembly of long filaments. Thus, we favor the parallel dimer intermediate assembly model involving head-to-tail interactions.

Head-to-tail interactions, while unprecedented in myosins, are particularly intriguing since such interactions have been observed for skeletal muscle tropomyosin [26]. Structurally, tropomyosin is similar to the myosin II rod domain in that it is a relatively long dimeric parallel coiled coil without a globular headgroup. It has an almost perfect heptad-repeating pattern and contains many charged residues in the solvent-exposed positions of the coiled coil. Filament formation in tropomyosin also depends on salt in the same way that myosin does [27], suggesting an important role for electrostatic interactions [28–30]. In addition to the expected distribution of amino acids within the heptad repeating unit, other, larger-scale sequence features exist in common between the tropomyosin and the myosin coiled coil domains; these include 28-amino acid and 196-amino acid repeating units as defined by charged amino acids [28]. McLachlan and Stewart [31] predicted that tropomyosin has two 9-amino acid stretches that lie near the N and C termini that are involved in head-to-tail polymerization. Nevertheless, since these sequence-repeating patterns are found throughout the coiled coil domains of both tropomyosin and myosin, perhaps it is not surprising that electrostatic interactions could foster the formation of a wide variety of self-assembling structures. It has been suggested that the headgroups in myosin are critical for directing self-assembly to form correctly functional polymers and perhaps we have found yet another self-assembled structure that is possible when such structure-guiding headgroups are removed.

In conclusion, we find that a careful quantitative approach to AFM image analysis allows for the teasing out of features in the sub nanometer range—hitherto inaccessible from a qualitative approach to AFM imaging of protein samples. This approach has allowed us to elucidate a plausible model for the novel filament structures that we have observed for the *A. castellanii* type II myosin rod domain, grounded in assembly models proposed in the literature. Our results emphasize the importance of the highly regulated control that is necessary in the assembly of coiled coils that is required when electrostatic interactions are used as a driving force for higher order assembly; such chemical forces are well known to cause problems with nonspecific aggregation in proteins.

Acknowledgment

We thank Tom Pollard for discussions about myosin self-assembly, Al Schwab for discussions on general polymer theory, Ed Korn for the expression construct, and Lawrence Lee and Ian Pitha-Rowe for development of protein purification protocols. We gratefully acknowledge support from NSF Grants MCB-9817188MCB-0211754 (R.F.) and DMS-9973258DMS-0314739 (R.S.M.) and a grant from the David and Lucile Packard Foundation. C.D.L. gratefully acknowledges a fellowship from the Howard Hughes Medical Institute.

References

[1] T.D. Pollard, Structure and polymerization of *Acanthamoeba* myosin-II filaments, J. Cell Biol. 95 (1982) 816–825.
[2] E. Reisler, C. Smith, G. Seegan, Myosin minifilaments, J. Mol. Biol. 143 (1980) 129–145.
[3] E. Reisler, P. Cheung, N. Borochov, Macromolecular assemblies of myosin, Biophys. J. 49 (1986) 335–342.
[4] K.M. Trybus, S. Lowey, Conformational states of smooth muscle myosin. Effects of light chain phosphorylation and ionic strength, J. Biol. Chem. 259 (1984) 8564–8571.
[5] R. Ward, P.M. Bennett, Paracrystals of myosin rod, J. Muscle Res. Cell Motil. 10 (1989) 34–52.
[6] J.H. Sinard, W.F. Stafford, T.D. Pollard, The mechanism of assembly of *Acanthamoeba* myosin-II minifilaments: minifilaments assemble by three successive dimerization steps, J. Cell Biol. 109 (1989) 1537–1547.
[7] J. Kuznicki, G.P. Cote, B. Bowers, E.D. Korn, Filament formation and actin-activated ATPase activity are abolished by proteolytic removal of a small peptide from the tip of the tail of the heavy chain of *Acanthamoeba* myosin II, J. Biol. Chem. 260 (1985) 1967–1972.
[8] M.A.L. Atkinson, E. Appella, M.A. Corigliano-Murphy, E.D. Korn, Enzymatic activity and filament assembly of *Acanthamoeba* myosin II are regulated by adjacent domains at the end of the tail, FEBS Lett. 234 (1988) 435–438.
[9] D.L. Rimm, D.A. Kaiser, D. Bhandari, P. Maupin, D.P. Kiehart, T.D. Pollard, Identification of functional regions on the tail of *Acanthamoeba* myosin-II using recombinant fusion proteins, I. High resolution epitope mapping and characterization of monoclonal antibody binding sites, J. Cell Biol. 111 (1990) 2405–2416.
[10] J.H. Sinard, D.L. Rimm, T.D. Pollard, Identification of functional regions on the tail of *Acanthamoeba* myosin-II using recombinant fusion proteins. II. Assembly properties of tails with NH_2- and COOH-terminal deletions, J. Cell Biol. 111 (1990) 2417–2426.
[11] J.A. Hammer, B. Bowers, B.M. Paterson, E.D. Korn, Complete nucleotide sequence and deduced polypeptide sequence of a nonmuscle myosin heavy chain gene from Acanthamoeba: evidence of a hinge in the rodlike tail, J. Cell Biol. 105 (1987) 913–925.
[12] M. Zolkiewski, M.J. Redowicz, E. Korn, J. Hammer, A. Ginsburg, Two-state thermal unfolding of a long dimeric coiled-coil: the *Acanthamoeba* myosin II rod, Biochemistry 36 (1997) 7876–7883.
[13] M. Taniguchi, O. Matsumoto, S. Suzuki, Y. Nishino, A. Okuda, T. Taga, T. Yamane, MgATP-induced conformational changes in a single myosin molecule observed by atomic force microscopy: periodicity of substructures in myosin rods, Scanning 25 (2003) 223–229.

[14] Y. Zhang, Z. Shao, A.P. Somlyo, A.V. Somlyo, Cryo-atomic force microscopy of smooth muscle myosin, Biophys. J. 72 (1997) 1308–1318.
[15] P. Hallett, G. Offer, M.J. Miles, Atomic force microscopy of the myosin molecule, Biophys. J. 68 (1995) 1604–1606.
[16] M. Walker, P. Knight, J. Trinick, Negative staining of myosin molecules, J. Mol. Biol. 184 (1985) 535–542.
[17] T.M. Laue, B.D. Shah, T.M. Ridgeway, S.L. Pelletier, Computer-aided interpretation of analytical sedimentation data for proteins, in: S. Harding, A. Rowe, A.J. Horton (Eds.), Analytical Ultracentrifugation in Biochemistry and Biopolymer Science, Royal Society of Chemistry, Cambridge, 1992, pp. 90–125.
[18] M.L. Johnson, J.J. Correia, D.A. Yphantis, H.R. Halvorson, Analysis of data from the analytical ultracentrifuge by nonlinear least-squares techniques, Biophys. J. 36 (1981) 575–588.
[19] U.W. Gedde, *Polymer Physics*, Chapter 4, Chapman & Hall, London, 1995.
[20] B.C. Hathorn, B.G. Sumpter, D.W. Noid, On the distribution of fragment sizes in the fragmentation of polymer chains, Macromol. Theory Simul. 10 (2001) 587–591.
[21] A.D.L. Humphris, A.N. Round, M.J. Miles, Enhanced Imaging of DNA via active quality factor control, Surface Sci. 491 (2001) 468–472.
[22] D.J. Keller, F.S. Franke, Envelope reconstruction of probe microscope images, Surface Sci. 294 (1993) 409–419.
[23] M.N. Murray, H.G. Hansma, M. Bezanilla, T. Sano, D.F. Ogletree, W. Kolbe, C.L. Smith, C.R. Cantor, S. Spengler, P.K. Hansma, M. Salmeron, Atomic force microscopy of biochemically tagged DNA, Proc. Natl. Acad. Sci. USA 90 (1993) 3811–3814.
[24] J. Vesenka, S. Manne, R. Giverson, T. Marsh, E. Henderson, Colloidal gold particles as an incompressible atomic force microscopy imaging standard for assessing the compressibility of biomolecule, Biophys. J. 65 (1993) 992–997.
[25] J.S. Davis, J. Buck, E.P. Greene, The myosin dimer: an intermediate in the self-assembly of the thick filament of vertebrate skeletal muscle, FEBS Lett. 140 (1982) 293–297.
[26] W.D. McCubbin, C.M. Kay, Physicochemical studies on the aggregation of bovine cardiac tropomyosin with ionic strength, Can. J. Biochem. 47 (1969) 411–414.
[27] A.D. Sousa, C.S. Farah, Quantitative analysis of tropomyosin linear polymerization equilibrium as a function of ionic strength, J. Biol. Chem. 277 (2002) 2081–2088.
[28] A.D. McLachlan, M. Stewart, The 14-fold periodicity in alpha-tropomyosin and the interaction with actin, J. Mol. Biol. 103 (1976) 271–298.
[29] D.A.D. Parry, Structure of rabbit skeletal myosin. Analysis of the amino acid sequences of two fragments from the rod region, J. Mol. Biol. 153 (1981) 459–464.
[30] A.D. McLachlan, J. Karn, Periodic features in the amino acid sequence of nematode myosin rod, J. Mol. Biol. 164 (1983) 605–626.
[31] A.D. McLachlan, M. Stewart, Tropomyosin coiled-coil interactions: evidence for an unstaggered structure, J. Mol. Biol. 98 (1975) 293–304.